https://doi.org/10.1016/j.cej.2020.126967

Co/Co_3O_4-embedded N-doped Hollow Carbon Composite derived from a Bimetallic MOF/ZnO Core-shell Template as a Sulfur Host for Li-S Batteries

Youngmoo Jeon,[1,†] Jeongyeon Lee,[2,†] Hakrae Jo,[1] Hwichan Hong,[1] Lawrence Yoon Suk Lee,[2,3,] Yuanzhe Piao[1,]**

[1] Department of Transdisciplinary Studies, Graduate School of Convergence Science and Technology, Seoul National University, Republic of Korea

[2] Department of Applied Biology and Chemical Technology and the State Key Laboratory of Chemical Biology and Drug Discovery, The Hong Kong Polytechnic University, Hung Hom, Kowloon, Hong Kong SAR, China

[3] Research Institute for Smart Energy, The Hong Kong Polytechnic University, Hung Hom, Kowloon, Hong Kong SAR, China

[†] These authors contributed equally to this work.

Corresponding authors

* Yuanzhe Piao, E-mail: parkat9@snu.ac.kr

* Lawrence Yoon Suk Lee, E-mail: lawrence.ys.lee@polyu.edu.hk

Highlights

- Zn/Co bimetallic MOFs/ZnO nanospheres core/shell structure was synthesized.

- Co/Co_3O_4 NPs-embedded N-doped hollow carbon composite (Co/Co_3O_4-NHC) was fabricated.

- Co/Co_3O_4-NHC provided abundant active sites and strong chemical adsorption with LiPSs.

- S@Co/Co_3O_4-NHC exhibited an outstanding rate capability and cycle stability in Li-S batteries.

Abstract

Lithium-sulfur batteries are a promising next-generation energy storage technology. To meet the industrial requirements, however, effective sulfur host materials are highly desired for the enhanced sulfur loading and lithium polysulfides (LiPSs) trapping. Herein, we describe the synthesis of N-doped hollow carbon composite embedded with well-dispersed Co/Co_3O_4 nanoparticles (Co/Co_3O_4-NHC) via the carbonization of a Zn/Co bimetallic metal-organic frameworks/ZnO nanospheres core-shell structure. The Co/Co_3O_4-NHC features uniform N-doping, intertwined carbon nanotubes (CNTs), and dual types of pores. ZnO nanospheres employed as a template for hollow structure also contribute to the formation of CNTs and micro-pores. The S-infiltrated Co/Co_3O_4-NHC cathode delivers an excellent rate performance (specific capacity of 447.9 mA h g^{-1} at 5 C-rate) and stability (553.4 mA h g^{-1} after 500 cycles). With a high S loading (4 mg cm^{-2}), 87.8% of specific capacity is retained after 250 cycles. This work can offer insights on designing the sulfur host materials for high-performance Li-S batteries.

Keywords: lithium sulfur battery; cathode; zinc oxide nanosphere; cobalt oxide nanoparticle; ZIF-67

1. Introduction

Rechargeable batteries are one of the pivotal technologies for developing eco-friendly electric vehicles and energy storage devices. Currently, lithium-ion-based cathodes are dominating the rechargeable battery industry, yet their high cost and limited energy density have become a bottleneck for further advancement [1-3]. On the other hand, lithium-sulfur (Li-S) batteries have received much attention as a potential alternative energy storage system, owing to their high theoretical capacity (1675 mA h g^{-1}) and natural abundance of S [4-8]. Until now, the commercialization of Li-S batteries is still challenged by major technical issues: the low charge transfer kinetics due to poor electrical conductivity of S and lithium sulfide (Li_2S) [9-11]; the drastic volume expansion of S during charge/discharge cycling; and the shuttling of lithium polysulfides (LiPSs) which causes severe dissolution and diffusion of LiPSs into the electrolyte, leading to capacity fading and low coulombic efficiency [12-14]. It is highly demanded to develop an effective host material for S which can provide good ion and electron conductivity, accommodate the volume expansion, and suppress the LiPSs diffusion.

The initial strategy to alleviate these problems involves the molten sulfur that was infiltrated into various carbon materials [15,16], such as carbon nanotubes [17-19] and porous carbon spheres [20-22], to improve the electrical conductivity and physically confine the LiPSs. However, the non-polar nature of carbon materials makes it difficult to prevent the dissolution of LiPSs. Although the chemical interactions between the LiPSs and the polar hosts [23-25], such as metal oxides [26-29] and chalcogenides [30,31] embedded in carbon materials, have been exploited to suppress the dissolution/diffusion of LiPSs, it is still challenging to evenly distribute the polar species on carbon materials, often facing the problem of aggregation as the cycle number increases. The homogeneous distribution of polar species is not only beneficial for the structural stability

during the extended cycling but also provides the rapid Li-ion and electron transport paths for high electrical and ionic conductivities. In this regard, metal-organic frameworks (MOFs) can be a suitable candidate due to their intrinsic porous structures and tunable chemical compositions [32-35]. For example, zeolitic imidazolate framework-67 (ZIF-67), composed of the tetrahedrally coordinated divalent Co^{2+} ions and imidazolate ligands, can effectively trap the LiPSs by strong chemical bonding with Co ions [36-39]. Direct use of ZIF-67 or their composites with conductive supports as a S host, however, still encounters the complications of low electric conductivity, large size, and the aggregation of Co atoms, which inevitably lead to the poor performance and capacity fading in long-term cycles [36]. Alternatively, MOFs have been widely employed as templates to prepare porous carbon materials embedded with metal oxides or heteroatoms that are advantageous in catalytic performance and protection of LiPSs [37-39].

Herein, we present the design and synthesis of Co/Co_3O_4 nanoparticles-embedded N-doped hollow carbon composite (Co/Co_3O_4-NHC) as an effective S hosting material for Li-S battery. By growing ZIF-67 on ZnO nanosphere, a core-shell structured template featuring a bimetallic Zn/Co-MOFs shell surrounding the ZnO core is prepared, which is further carbonized to yield a hollow carbon composite with the controlled particle size, large micro- and meso-pore spaces, and strong chemical affinity for LiPSs. The roles of ZnO and bimetallic Zn/Co-MOFs are systematically studied to understand the formation mechanism of evenly distributed Co/Co_3O_4 nanoparticles in the N-doped carbon matrix with abundant carbon nanotubes (CNTs). The Co/Co_3O_4-NHC is further engaged as a cathode in Li-S battery to investigate the effects of hierarchical porous structure and Co/Co_3O_4 nanoparticles in the battery performances including rate capability, cycling stability, and specific discharge capacity.

2. Experimental Section

Materials

Zinc acetate dihydrate ($ZnAc{\cdot}2H_2O$) was purchased from Aldrich Chemical Co., and diethylene glycol (DEG, 99%), N,N-dimethylformamide (DMF, 99.5%), cobalt(II) nitrate hexahydrate ($Co(NO_3)_2{\cdot}6H_2O$, 97%), sodium hydroxide (NaOH, 98%), and hydrochloric acid (HCl, 35-37%) were purchased from Samchun Co. 2-methylimidazole (2-MeIm, 99%) was purchased from ACROS Co. All the chemicals were used as received unless mentioned otherwise.

Preparation of ZnO nanospheres coated with Zn/Co-MOF (ZnO@Zn/Co-MOF)

ZnO nanospheres were first prepared by the polyol-mediated precipitation method. Briefly, $ZnAc{\cdot}2H_2O$ (1.97 g) was dispersed in 90 mL diethylene glycol and heated to 160 °C for 24 h under mild stirring. After cooling to room temperature, milky suspension was washed by centrifugation with deionized water several times and dispersed again in a mixed solvent of DMF/H_2O (256 mL, 3:1 of V/V). To this solution of ZnO nanospheres, 2-MeIm (5 mmol) was added and the mixture was sonicated for 10 min, followed by the addition of $Co(NO_3)_2{\cdot}6H_2O$ (0.17 mmol) under stirring. The mixed solution was then heated at 50 °C for 3 h and cooled to room temperature. The ZnO@Zn/Co-MOF nanocomposites were collected by centrifugation, washed several times with ethanol, and dried at 60 °C overnight.

Preparation of Co/Co_3O_4-NHC and NHC nanocomposites

The as-obtained ZnO@Zn/Co-MOF nanocomposites were annealed in a tube furnace at 920 °C for 5 h (heating rate = 2 °C/min) under an Ar atmosphere. The obtained black powder was immersed in 4 M NaOH for 24 h to remove the residual zinc. The product was collected by centrifugation, followed by repeated washing with water and ethanol, and freeze-drying for three days to minimize particle aggregation. This final product is denoted as Co/Co_3O_4-NHC. For

comparison, the as-prepared Co/Co_3O_4-NHC was immersed in 4 M HCl for 24 h to remove the Co_3O_4 nanoparticles, and the resulting product named as NHC.

Preparation of ZIF-67 and Co-NC

For the synthesis of ZIF-67, $Co(NO_3)_2 \cdot 6H_2O$ (4 mmol) and 2-MeIm (160 mmol) were dissolved in 10 mL and 200 mL of methanol, respectively. The $Co(NO_3)_2 \cdot 6H_2O$ solution was then poured into the 2-MeIm solution with vigorous stirring and the mixture was stirred for 24 h. The purple ZIF-67 was collected by centrifugation, washed with ethanol, and dried at 60 °C overnight. The as-obtained ZIF-67 was annealed at 920 °C for 5 h, and the final product was denoted as Co-NC.

Sulfur impregnation of Co/Co_3O_4-NHC (S@Co/Co_3O_4-NHC)

Sulfur was impregnated into the as-prepared Co/Co_3O_4-NHC (S@Co/Co_3O_4-NHC) via the typical melting-diffusion method. The Co/Co_3O_4-NHC and S powder were mixed in a weight ratio of 3:7, and heated to 155 °C for 12 h in a tube furnace under an Ar atmosphere. For comparison, the same method was engaged to impregnate S to NHC (S@NHC) and Co-NC (S@Co-NC).

Preparation of Li_2S_6 solution

For the LiPSs adsorption test, a 10 mM Li_2S_6 solution was prepared by mixing the sulfur and Li_2S with a molar ratio of 5:1 in a mixed solvent of 1,3-dioxolane and 1,2-dimethoxyethane with a weight ratio of 1:1 under vigorous stirring at 60 °C for 24 h in the glovebox.

Material characterizations

The morphology of the as-prepared samples was characterized using field emission scanning electron microscopy (FE-SEM, Hitachi S-4800) and transmission electron microscopy (TEM, JEM-2010, JEOL) equipped with an energy-dispersive X-ray (EDX) spectrometer. The crystalline structures of the samples were characterized using an X-ray diffractometer (D8 Advance, Bruker) with Cu Kα (λ = 1.5406 Å) radiation. Raman spectra were collected using a Raman spectrometer

(DXR2xi Raman Imaging Microscope, Thermo Scientific) with an excitation laser wavelength of 532 nm. N_2 adsorption-desorption isotherms were obtained using an adsorption analyzer (BELSORP-mini II, MicrotracBEL Corp.). Thermogravimetric analysis (TGA) was performed using a thermal analyzer (TGA/DSC 1, Mettler Toledo Co.) at a heating rate of 10 °C min^{-1} in N_2 or air atmosphere. X-ray photoelectron spectroscopy (XPS) analysis was carried out using an X-ray photoelectron spectrometer (AXIS-HSi, Kratos Analytical) with a Mg Kα X-ray source.

Electrochemical measurements

The working electrodes were prepared by mixing the S@Co/Co_3O_4-NHC composite, a conducting agent (Super P), and a binder (polyvinylidene difluoride) in N-methyl-2-pyrrolidinone with a weight ratio of 8:1:1 using a ball-miller (Mini-Mill PULVERISETTE 23, FRITSCH). After mixing, the slurry was cast onto an Al foil using a doctor blade, and then dried at 60 °C to remove the solvent. The as-prepared electrode was cut in a circular shape, and the mass loading of the active materials in the electrode was approximately 1.2 mg cm^{-2}. The electrochemical performances were tested with a CR 2016 coin-type cell using Li metal as the counter and reference electrodes and Celgard 2450 as the separator. Bis(trifluoromethane) sulfonimide lithium salt (1.0 M) in a mixed solvent of 1,3-dioxolane and 1,2-dimethoxyethane with a weight ratio of 1:1 was used as an electrolyte with 1 wt% $LiNO_3$ additive. The amount of electrolyte was fixed to 30 μL mg^{-1} for all the cells prepared. The coin-cell was assembled in an Ar-filled glovebox with moisture and oxygen contents below 1 ppm. Galvanostatic charge and discharge tests were conducted using a WBCS3000S cycler (WonATech Co.) at different current densities in a voltage range of 1.7–2.8 V (vs. Li/Li^+). Cyclic voltammograms (CV) were measured from 1.7 to 2.8 V (vs. Li/Li^+) at various scan rates from 0.1 to 1.0 mV s^{-1}. Electrochemical impedance spectroscopy (EIS) was performed

using a ZIVE SP1 potentiostat (ZIVE LAB, WonATech Co.) in a frequency range from 0.1 to 100 kHz.

3. Results and Discussion

Figure 1a illustrates the synthetic strategy of the hollow N-doped carbon composites embedded with Co/Co_3O_4 nanoparticles. Using the polyol-mediated precipitation method [40], we first synthesized ZnO nanospheres as both a sacrificial template and the zinc source for binary Zn/Co-metal-organic frameworks (MOFs). During the MOF formation in the presence of as-prepared ZnO nanospheres, the organic linker molecule (2-MeIm) coordinates to Co and Zn ions, forming the bimetallic Zn/Co-MOFs that encapsulate the ZnO nanosphere core (ZnO@Zn/Co-MOFs). In the subsequent thermal treatment at 920 °C, the organic linkers and Co ions in Zn/Co-MOFs are reduced to *in situ* form N-doped carbon and Co/Co_3O_4 nanoparticles, respectively. Simultaneously, the N-doped carbons in the vicinity of Co/Co_3O_4 nanoparticles are converted to carbon nanotubes (CNTs) catalyzed by Co nanoparticles [38,41,42]. Meanwhile, the Zn species, both in the Zn/Co-MOFs and ZnO core, is first reduced to metallic Zn that eventually vaporizes at a higher temperature (boiling point of Zn = 907 °C) [40], which also facilitates the growth of CNT in Co/Co_3O_4-embedded N-doped hollow carbon composite (denoted as Co/Co_3O_4-NHC).

The morphology and composition of as-prepared samples were examined by a combination of microscopic techniques. Figure S1a in the Supporting Information is the field emission-scanning electron microscopic (FE-SEM) image of ZnO nanospheres, which displays uniform spherical nanoparticles with an average diameter of ca. 150 nm. A high-magnification image (Figure S1b) reveals that the ZnO nanospheres are composed of numerous smaller nanoparticles ($d < 10$ nm) thus rendering a rough surface. The encapsulation of ZnO with Zn/Co-MOFs is evident in the FE-SEM images of ZnO@Zn/Co-MOFs (Figure 1b and 1c), where the brighter color in the center

suggests the formation of core-shell structure. A non-conventional morphology of ZnO@Zn/Co-MOF (d = ca. 350 nm) features the uneven surface with overlapping polyhedrons, probably due to the concurrent growth of MOFs at multiple sites or secondary growth on a pre-formed MOFs. The transmission electron microscopic (TEM) image presented in Figure 1d confirms that the ZnO core is well-encapsulated by the Zn/Co-MOF shell (ca. 100 nm thick), retaining its size and morphology unchanged. The elemental distribution, revealed by energy-dispersive X-ray (EDX) elemental mapping, further verifies the structure of ZnO@Zn/Co-MOFs (Figure 1e). The C, N, and Co are evenly distributed in the shell region, whereas Zn is more concentrated in the core area, which strongly supports that the Zn ions are partially dissolved from ZnO nanospheres and coordinated with 2-MeIm in the MOF formation step.

The MOFs can be used as a precursor to obtain the carbon materials doped with the desired heteroatoms by a simple annealing process. The morphology of ZnO@Zn/Co-MOFs has drastically changed upon the thermal and base treatments. As shown in Figure 2a and 2b, the multi-edged polygonal shell of ZnO@Zn/Co-MOFs has changed to an irregular spherical shape of which surface is covered with worm-like structures and smaller nanoparticles. TEM analysis confirms these structural and morphological changes with clear visualization of tubular structures and nanoparticles (Figure 2c and S2). The contrast difference between the center (lighter) and rim (darker) regions indicates the hollow structure of Co/Co_3O_4-NHC, where the shell thickness has declined to ca. 80 nm. The elemental mappings of Co/Co_3O_4-NHC indicate that C, N, O, and Co are well-distributed over the entire composite, whereas Zn has almost disappeared due to the thermal and base treatments (Figure 2d and S3). High-resolution TEM (HR-TEM) image and the corresponding fast Fourier transform (FFT) pattern (Figure 2e) give the crystal structural information of nanoparticles in Co/Co_3O_4-NHC shell. The lattice spacings of 0.202 and 0.205 nm

observed in different nanoparticles correspond to the (400) plane of Co_3O_4 and the (111) plane of metallic Co, respectively, indicating the existence of Co_3O_4 nanoparticles with some metallic Co species. The ZnO nanoparticle plays a critical role in constructing such a unique morphology of Co/Co_3O_4-NHC (Figure 2f). First, upon the thermal treatment, the ZnO core is reduced to metallic Zn and evaporates, leaving a void space. Second, the interaction with 2-MeIm allows the formation of bimetallic Zn/Co-MOFs, in which Zn species is also reduced and vanishes during the thermal treatment, creating micropores in the shell. Meanwhile, the oxygen gas released from ZnO can partially oxidize the metallic Co present in the shell, yielding a Co/Co_3O_4 nanoparticle-embedded hollow N-doped carbon composite. Third, the evaporation of Zn species from inside is also responsible for the formation of such intertwined CNTs, assisted by the catalytic reaction of Co nanoparticles at high temperature (920 °C) [38,41,42], which is generally not observed from the carbonization of pristine ZIF-67.

To investigate the role of Co/Co_3O_4 nanoparticles in the electrochemical performance of Li-S battery, we removed the Co_3O_4 nanoparticles by etching the Co/Co_3O_4-NHC with acid (denoted as NHC), as shown in Figure S4. The TEM image and the EDX elemental mapping shown in Figure S4 verify that most Co species disappeared, yet the morphology of NHC is unchanged. We also prepared the ZIF-67 nanocrystals which have the uniform and typical polyhedron morphology with the average size similar to Co/Co_3O_4-NHC (ca. 250 nm) [43] to investigate the role of ZnO nanospheres (Figure S5). The as-prepared ZIF-67 nanocrystals were annealed under the same conditions for comparison purpose, which is denoted as Co-NC (Figure S6). Notably, the size of Co-NC remains similar to the pristine ZIF-67 and a few CNTs are visible on the surface.

To confirm the crystal structure and composition of embedded nanoparticles, the X-ray diffraction (XRD) patterns of Co/Co_3O_4-NHC, NHC, and Co-NC are obtained and compared in

Figure 3a. Two types of diffraction peaks are identified from the Co/Co_3O_4-NHC, where those observed at 19.0°, 31.3°, 36.9°, 44.8°, 59.4°, 65.2°, and 77.3° correspond to the (111), (220), (311), (400), (511), (440), and (533) planes of spinel Co_3O_4 phase (JCPDS No. 42-1467), respectively, while another small diffraction peak at 44.2° can be ascribed to the (111) plane of cubic Co phase (JCPDS No. 15-0806). This confirms the HR-TEM results that identified Co_3O_4 nanoparticles with metallic Co nanoparticles, further indicating that the majority of metallic Co has been oxidized to Co_3O_4 during the heat treatment. There are no diffraction peaks related to metallic Zn or ZnO, indicating that Zn species has been removed from Co/Co_3O_4-NHC. The XRD pattern of NHC displays only the weak diffraction peaks of the (111) and (200) planes of cubic Co phase at 44.2° and 51.5°, respectively, suggesting a small number of Co nanoparticles still exist even after the acid treatment. In the case of Co-NC, cubic Co phase is recognized with the diffraction peaks at 44.2°, 51.5°, and 75.9° corresponding to the (111), (200), and (220) planes, respectively.

We also collected the Raman spectra to verify the chemical composition of the as-synthesized samples, which are compared in Figure 3b. From the spectrum of Co/Co_3O_4-NHC, four characteristic Raman peaks corresponding to the E_g, F_{2g}, and A_{1g} modes of crystalline Co_3O_4 are identified at 475, 515 and 611, and 679 cm^{-1}, respectively [44,45]. Two additional peaks at 1341 and 1590 cm^{-1} are assigned to the D (disordered carbon) and G bands (graphitic carbon) of carbon species, respectively. The Raman spectrum of NHC exhibits only the carbon-related peaks, suggesting that most of Co species are removed by the acid treatment. Similar to the Co/Co_3O_4-NHC, the Raman features of Co_3O_4 and carbon species are found from the Co-NC.

The synthesis of Co/Co_3O_4-NHC using the ZnO template allows the formation of hollow structure with extensive pores in the shell, which would largely benefit the performance as the sulfur host in Li-S battery. We evaluated the porosity of as-prepared samples by measuring the N_2

adsorption-desorption isotherms (Figure 3c). Both Co/Co_3O_4-NHC and NHC display a mixture of type I and type IV isotherms with a hysteresis loop, indicating the coexistence of meso- and micropores in their structures. The Brunauer-Emmett-Teller (BET) surface area and the total pore volume of Co/Co_3O_4-NHC are 453.6 m^2 g^{-1} and 0.72 cm^3 g^{-1}, respectively, while NHC shows the higher values of 588.0 m^2 g^{-1} and 0.93 cm^3 g^{-1}, respectively, as the removal of Co/Co_3O_4 nanoparticles results in increasing the volume of mesopores (Figure S7). Such hierarchical structure with two dimensions of pores can facilitate the diffusion of Li-ion and provide enough space for high sulfur loading. In the case of Co-NC, the BET surface area and total pore volume are measured to be 182.7 m^2 g^{-1} and 0.37 cm^3 g^{-1}, respectively, indicating the insufficient pore volume for sulfur loading.

As stated earlier, the Co/Co_3O_4 nanoparticles are known to effectively adsorb the LiPSs [39,46,47], which is a great advantage in developing the sulfur host for the high specific capacity and stable cyclability for Li-S battery. The amount of Co/Co_3O_4 in the samples was determined by thermogravimetric analysis (TGA) engaged in an air atmosphere (Figure 3d). The Co/Co_3O_4 contents in Co/Co_3O_4-NHC is estimated to be ca. 35 wt%, which is lower than Co contents of Co-NC (ca. 62 wt%). This is because the Co/Co_3O_4-NHC is fabricated from the bimetallic Zn/Co-MOFs in which Co ions are partially replaced by Zn ions from ZnO nanosphere, whereas the Co-NC is converted from Co-MOFs (ZIF-67). Meanwhile, the NHC has merely 6 wt% Co_3O_4 and Co nanoparticles due to the acid treatment, which is in good agreement with previous characterizations. Interestingly, the onset of weight loss in TGA analysis begins at much lower temperatures for Co/Co_3O_4-NHC and Co-NC compared to NHC. The Co_3O_4 and/or metallic Co nanoparticles in Co/Co_3O_4-NHC and Co-NC are believed to facilitate the oxidation of carbon materials, thus causing the earlier decomposition of carbon during TGA analysis [48].

We employed the X-ray photoelectron spectroscopy (XPS) to investigate the chemical composition and oxidation state of samples. The XPS survey spectrum of Co/Co_3O_4-NHC, shown in Figure S8a, confirms the presence of C, N, O, and Co. From the high-resolution C 1s XPS spectrum (Figure S8b), four peaks are observed at 284.7, 285.2, 286.8, and 288.2 eV corresponding to the sp^3 C, sp^2 C, C-O/C-N, and C=O, respectively. The high-resolution N 1s XPS spectrum (Figure 3e) shows the peaks at 398.7, 400.1, and 401.2 eV attributed to the pyridinic N (28.8 %), pyrrolic N (49.3 %), and graphitic N (21.9 %), respectively. The abundant pyridinic and pyrrolic N atoms are expected to enhance the cycle stability and electrical conductivity as they can provide the active sites for strong chemical adsorption of LiPSs [49-51]. The high-resolution Co $2p_{3/2}$ XPS spectrum (Figure 3f) can be deconvoluted into four peaks at 778.4, 780.2, 781.0, and 786.2 eV, which are assigned to the metallic Co, Co^{3+}, Co^{2+}, and satellite peaks, respectively. In addition to Co nanoparticles, the existence of Co_3O_4 is confirmed by these Co^{3+}, Co^{2+}, and satellite peaks [52,53]. It was reported that the Co/Co_3O_4 nanoparticles not only efficiently anchor and immobilize LiPSs but also accelerate the redox kinetics of LiPSs during cycling [39,47,54]. The decreased Co_3O_4 peak intensities are evident in the high-resolution Co $2p_{3/2}$ spectrum of NHC (Figure S9), which agrees well with the XRD results (Figure 3a). In contrast, the high-resolution N 1s XPS spectrum of NHC exhibits no obvious changes, confirming that the content and types of N-doping sites are retained after acid treatment (Figure S9c).

The S-infiltrated cathodes were prepared by impregnating Co/Co_3O_4-NHC, NHC, and Co-NC with S powder (S-to-host weight ratio = 7:3) by the typical melt-diffusion method (denoted as S@Co/Co_3O_4-NHC, S@NHC, and S@Co-NC, respectively). The SEM image in Figure S10a shows that the S@Co/Co_3O_4-NHC maintains its spherical morphology without any aggregated sulfur particles. Moreover, the TEM and EDX elemental mapping images in Figure S10b and S10c

show that sulfur powder was successfully diffused into the pores of Co/Co_3O_4-NHC. This is also supported by the XRD pattern (Figure S11) that displays the diffraction peaks for S (JCPDS No. 08-0247) and Co_3O_4 (JCPDS No. 42-1467). The SEM, TEM, and the EDX elemental mapping images of S@NHC (Figure S10d-f) show that sulfur powder was also diffused into the pores of NHC without any aggregated sulfur particles. The unchanged chemical composition of S@Co/Co_3O_4-NHC is confirmed by Raman and XPS survey spectra (Figure S12a and S12b). The XPS survey spectrum exhibits an additional S peak, and the high-resolution S 2p XPS spectrum (Figure S12c) shows two peaks at 163.5 and 164.7 eV attributed to S $2p^{3/2}$ and S $2p^{1/2}$ spin orbits, respectively, and another peak at 167.8 eV assigned to the sulfate due to oxidation of S in an air [55]. Upon the S impregnation, the BET surface area and the total pore volume of S@Co/Co_3O_4-NHC are substantially reduced to 7.0 m^2 g^{-1} and 0.07 cm^3 g^{-1} from 453.6 m^2 g^{-1} and 0.72 cm^3 g^{-1}, respectively, confirming the successful S loading in the Co/Co_3O_4-NHC (Figure S12d). The S contents of the composites measured by TGA in the N_2 atmosphere (Figure S13) are 71, 71, and 63 wt% in the S@Co/Co_3O_4-NHC, S@NHC, and S@Co-NC, respectively, indicating insufficient space in Co-NC for S loading, as shown in Figure S14.

To reveal the electrocatalytic effect of Co/Co_3O_4 nanoparticles, cyclic voltammetry (CV) was performed on two samples with comparable porosities but contrasting Co/Co_3O_4 contents, S@Co/Co_3O_4-NHC and S@NHC, within the voltage range of 1.7 and 2.8 V at different scan rates (Figure 4a and S15). At a slow scan rate of 0.1 mV s^{-1}, two cathodic peaks appear in the CVs of both S@Co/Co_3O_4-NHC and S@NHC; one located at ca. 2.26 V and the other at ca. 2.00 V, which arise from the reduction of S to high-order LiPSs (Li_2S_x, $4 \leq x \leq 8$) and the further reduction of these polysulfides to solid-state Li_2S_2/Li_2S, respectively. The anodic peaks located at ca. 2.40 V indicate the oxidation of Li_2S_2/Li_2S back to S. In both electrodes, peak separation is observed as

the scan rate increases. In the case of S@Co/Co_3O_4-NHC, two cathodic peaks are negatively shifted by 0.03 and 0.10 V while the anodic peak is positively shifted by 0.11 V. Similar peak shifts are observed from S@NHC but with larger extents (0.05 and 0.12 V for cathodic peaks and 0.16 V for anodic peak). This implies that the Co/Co_3O_4 nanoparticles can effectively decrease the polarization activation and enhance the redox kinetics.

The redox kinetics of both electrodes are further analyzed by the Randles–Sevcik equation (1) [56-58]:

$$I_p = (2.69 \times 10^5) n^{1.5} A D_{Li}^{0.5} C_{Li} \nu^{0.5} \quad (1)$$

where I_p is the peak current, n is the number of electrons transferred, A is the surface area of the electrode, D_{Li} is the Li-ion diffusion coefficient, C_{Li} is the Li-ion concentration in the electrolyte, and ν is the scan rate. The cathodic and anodic D_{Li} values of the two electrodes are calculated from the linear relationship of I_p vs. $\nu^{0.5}$, as compared in Figure 4b, 4c and S16. The S@Co/Co_3O_4-NHC exhibits the steeper slopes than S@NHC for both cathodic and anodic peaks, indicating the higher Li-ion diffusivity due to the chemical affinity of Co/Co_3O_4 nanoparticles, thus providing the faster kinetics during cycling.

The electrochemical impedance spectroscopy (EIS) can provide further insights into the electrochemical kinetics. Figure S17 shows the Nyquist plots of Co/Co_3O_4-NHC and NHC electrodes that are freshly prepared to fabricate the symmetric cells with the electrolyte containing 10 mM Li_2S_6. The smaller semicircle (12.2 ± 0.4 Ω) observed from Co/Co_3O_4-NHC electrode reflects the lower charge transfer resistance (R_{ct}) in the high-frequency region, compared with NHC (24.2 ± 0.5 Ω). Combined with CV results, the Co/Co_3O_4 nanoparticles in the S@Co/Co_3O_4-NHC are found to play crucial roles in enhancing the redox kinetics and facilitating the conversion of polysulfides to LiPSs, as well as fast electron transport.

The rate performances of the S@Co/Co_3O_4-NHC, S@NHC, and S@Co-NC cathodes are tested at various current densities from 0.2 to 7 C, as shown in Figure 4d. The S@Co/Co_3O_4-NHC cathode exhibits good specific discharge capacities of 957.1, 776.6, 658.9, 538.2, 494.4, 447.9, and 423.0 mA h g^{-1} at 0.2, 0.5, 1, 2, 3, and even at high current densities of 5 and 7C, respectively, while the S@NHC cathode exhibits the lower specific discharge capacities. The enhanced rate capability of S@Co/Co_3O_4-NHC cathode is attributed to the presence of Co/Co_3O_4 nanoparticles that enable the fast LiPSs redox kinetics, as revealed with CV and EIS results. Moreover, the discharge capacity of the S@Co/Co_3O_4-NHC cathode is recovered to 886.4 mA h g^{-1} when the current density returns to 0.2 C, indicating good structural stability of S@Co/Co_3O_4-NHC composites. The corresponding charge/discharge profiles of the samples are presented in Figure 4e and S18. Two distinct discharge and charge plateaus are evident in S@Co/Co_3O_4-NHC cathode even at high current densities. In contrast, at high current densities of 5 and 7C, these plateaus are not observed from the S@NHC cathode due to the slow kinetics of the LiPSs conversion. Moreover, the S@Co-NC cathode shows the large polarization due to the small surface area that limits the active sites and the utilization of sulfur. We also evaluated the cycling performance of the S@Co/Co_3O_4-NHC cathode with a higher sulfur loading of 4 mg cm^{-2} at 1C rate (Figure 4f). The specific discharge capacity increases during the initial ten cycles due to the activation of high-loaded electrode. The corresponding galvanostatic discharge/charge profiles of the high loading S@Co/Co_3O_4-NHC cathode (Figure S19) also display a similar activation process for the initial ten cycles followed by a stable cyclability till 250 cycles. The specific discharge capacity of 371.9 mA h g^{-1} is still maintained after 250 cycles with a capacity retention of 87.8%, corresponding to a low capacity decay of 0.048% per cycle. Figure 4g displays the long-term cycling performances of the S@Co/Co_3O_4-NHC, S@NHC, and S@Co-NC cathodes evaluated at 1C. The S@Co/Co_3O_4-

NHC cathode exhibits the best cycling stability as manifested by a high discharge capacity of 553.4 mA h g^{-1} after 500 cycles with a capacity retention of 84.1%. The corresponding charge/discharge profiles of the S@Co/Co_3O_4-NHC (Figure S20) show two distinct discharge and charge plateaus, confirming a stable cyclability. On the other hand, S@NHC cathode has a discharge capacity of 439.1 mA h g^{-1} after 500 cycles with the lowest capacity retention of 74.2% due to the low chemical affinity with LiPSs resulting in the largest capacity fading during long-term cycling. Moreover, S@Co-NC cathode has a discharge capacity of 356.9 mA h g^{-1} after 500 cycles with a capacity retention of 79.7%, showing higher capacity retention than the S@NHC cathode benefited by the presence of Co nanoparticles in the composites. Although some Co nanoparticles in S@Co-NC can suppress the dissolution of LiPSs, the insufficient surface area results in low utilization of sulfur and the lowest discharge capacity. These results clearly indicate that the S@Co/Co_3O_4-NHC cathode not only immobilizes the LiPSs with strong chemical affinity by introducing Co/Co_3O_4 nanoparticles but also provides large surface area for high utilization of sulfur, showing the improved long-term cycling performance.

To verify the chemical affinity of the synthesized materials for LiPSs, a polysulfide adsorption test was conducted using the Li_2S_6 solution by monitoring the concentration of Li_2S_6 using UV-vis absorption spectroscopy. As shown in Figure 4h, 10 mM Li_2S_6 solution containing Co/Co_3O_4-NHC becomes almost colorless after stirring for 24h, exhibiting the significantly decreased absorption peaks in the visible region, whereas the Li_2S_6 solution with NHC remains light yellow. The soluble LiPSs are partially entrapped in the NHC due to the chemical adsorption on N, but it is insufficient to encapsulate the most LiPSs within the composite. In contrast, Co/Co_3O_4-NHC effectively entraps the LiPSs with the synergistic effect of N doping and Co/Co_3O_4 nanoparticles, showing the stronger chemical interaction with LiPSs. In addition, we examined the separators and

S@Co/Co_3O_4-NHC and S@NHC cathodes after 100 cycles. The digital photo of the separators disassembled from the cycled cells provides the visual evidence of severe dissolution of the LiPSs only from the S@NHC cell (Figure S21a). Furthermore, the cycled S@Co/Co_3O_4-NHC cathode well retains its morphology (Figure S21b), demonstrating that Co/Co_3O_4-NHC composites can effectively suppress the dissolution of the LiPSs. In contrast, the initial morphology of S@NHC cathode has largely altered with irregular discharge products covering the surface (Figure S21c) because of the insufficient chemical adsorption affinity for the LiPSs, which explains its poor electrochemical performance.

4. Conclusion

In summary, N-doped hollow and porous carbon composites containing Co/Co_3O_4 nanoparticles and CNTs (Co/Co_3O_4-NHC) are prepared as an effective S hosting material for Li-S battery. The ZnO nanospheres used as a sacrificial template and Zn precursor for bimetallic MOFs are reduced and evaporate during the carbonization to yield the hierarchical porous carbon structures in which Co/Co_3O_4 nanoparticles are evenly distributed. The use of ZnO also facilitated the *in situ* growth of CNTs, as well as the micropores, which physically confine the LiPSs and enhance the Li-ion and electron transports. Moreover, the carbonization of bimetallic Co/Zn-MOFs afforded evenly distributed Co/Co_3O_4 nanoparticles in the N-doped carbon matrix, providing abundant active sites to accelerate the S redox reactions and chemically interact with LiPSs, thus preventing the dissolution and diffusion of LiPSs. An outstanding rate capability (447.9 mA h g^{-1} at 5 C rate) and good cycling stability (553.4 mA h g^{-1} after 500 cycles at 1 C rate) are demonstrated based on S@Co/Co_3O_4-NHC cathode. Also, with a higher S loading (4 mg cm^{-2}), a stable specific discharge capacity of 371.9 mA h g^{-1} is retained after 250 cycles with a capacity retention of 87.8%. This

work can offer a promising strategy to develop high-performance Li-S batteries and other catalysis-related applications.

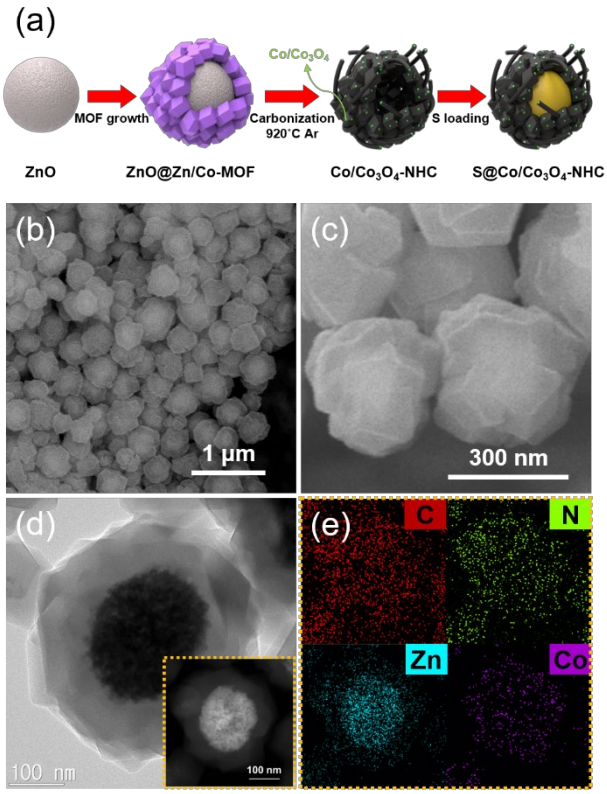

Figure 1. (a) Schematic illustration of the synthetic procedure for S@Co/Co_3O_4-NHC. (b) Low- and (c) high-magnification FE-SEM images, (d) TEM image, and (e) EDX elemental mapping images of ZnO@Zn/Co-MOF. The inset in (d) is the STEM image.

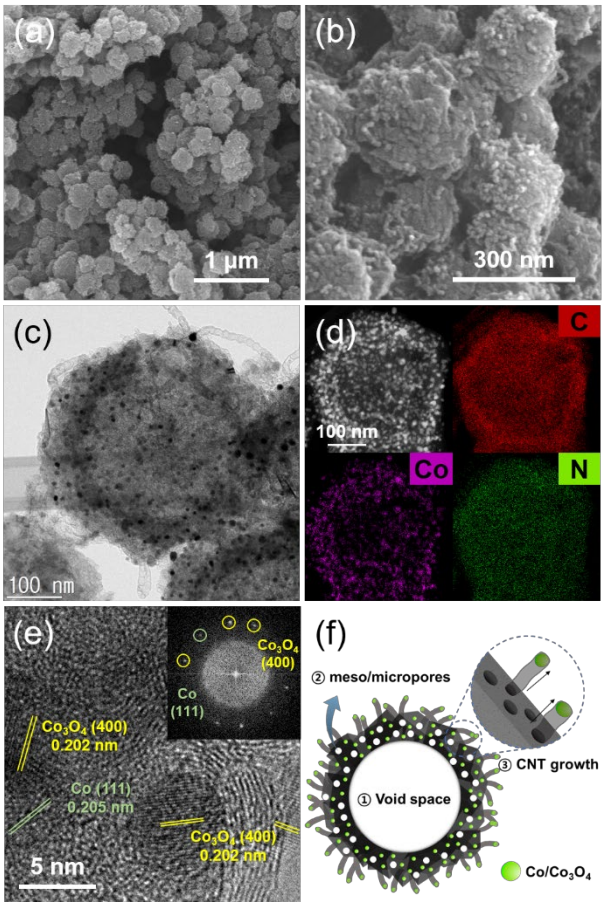

Figure 2. (a) Low- and (b) high-magnification FE-SEM images, (c) TEM image, (d) EDX elemental mapping images, and (e) HR-TEM image of Co/Co_3O_4-NHC. The inset in (e) is the corresponding FFT image. (f) Schematic illustrating the effective roles of ZnO core in the synthetic process of Co/Co_3O_4-NHC.

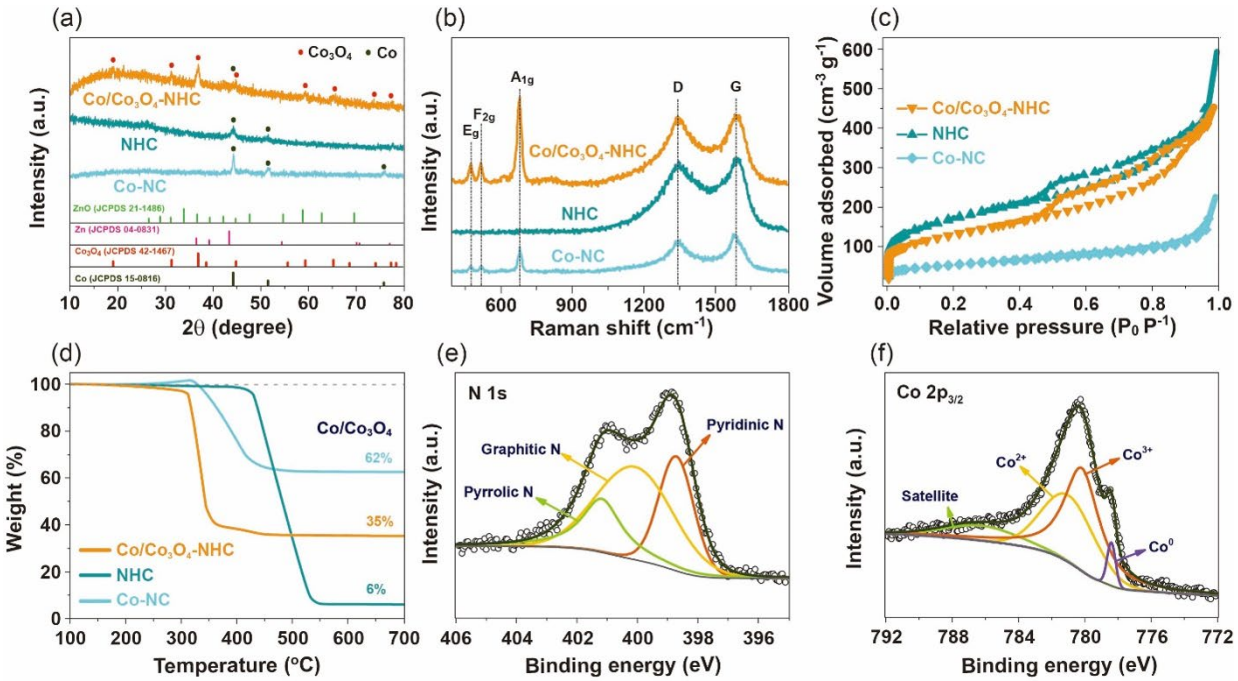

Figure 3. (a) XRD patterns, (b) Raman spectra, (c) N_2 adsorption-desorption isotherms, and (d) TGA curves of Co/Co_3O_4-NHC, NHC, and Co-NC. High-resolution XPS spectra for (e) N 1s and (f) Co $2p_{3/2}$ regions of Co/Co_3O_4-NHC.

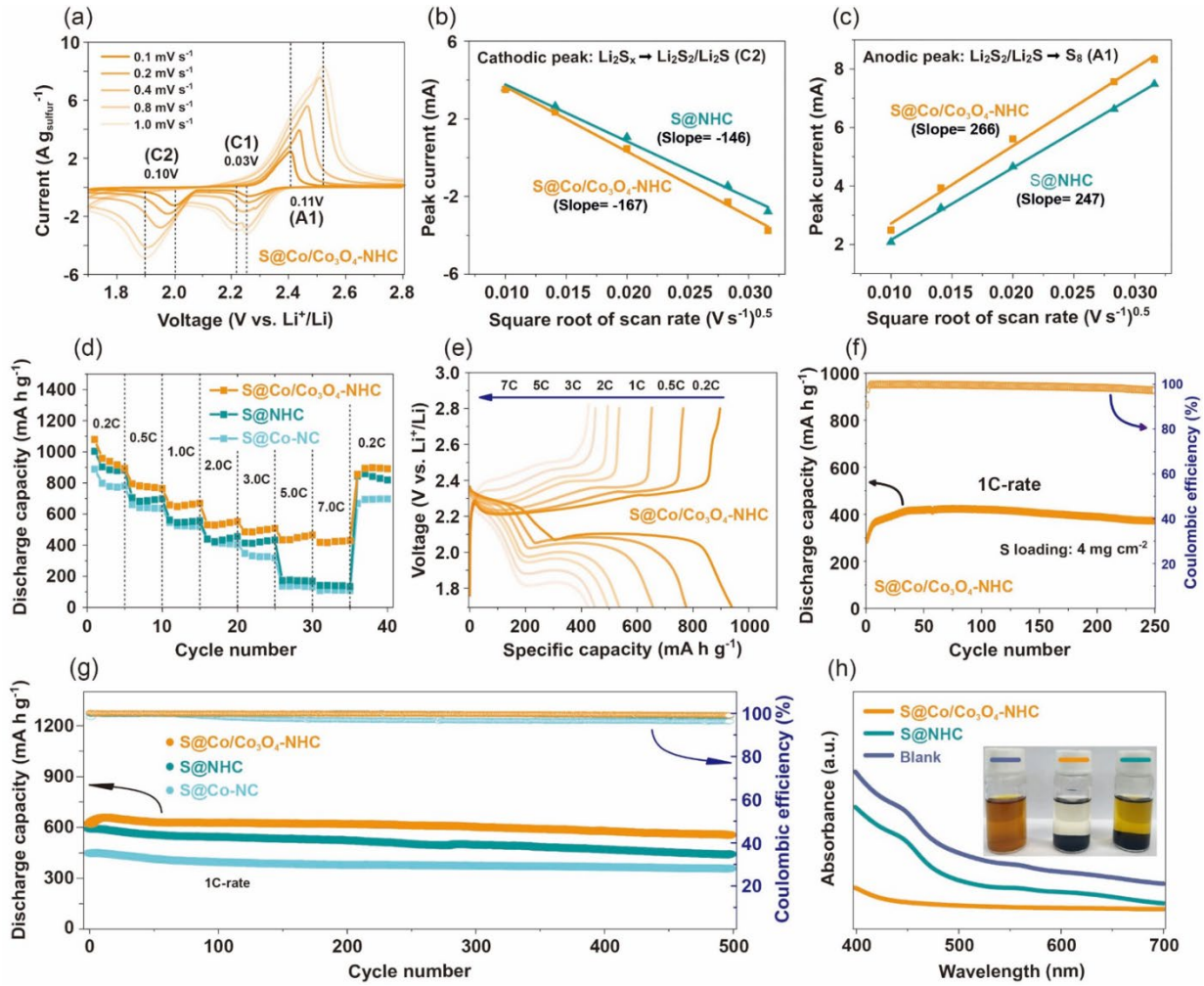

Figure 4. (a) CV curves of S@Co/Co_3O_4-NHC electrode at various scan rates from 0.1 to 1.0 mV s^{-1}. Plots of CV peak current of the (b) cathodic peak (Li_2S_X→Li_2S_2/Li_2S) and (c) anodic peak (Li_2S_2/Li_2S→S_8) against the square root of scan rate for the S@Co/Co_3O_4-NHC and S@NHC electrodes. (d) Rate performance of S@Co/Co_3O_4-NHC, S@NHC, and S@Co-NC electrodes. (e) Galvanostatic discharge/charge profiles of S@Co/Co_3O_4-NHC electrode at various current densities from 0.2 to 7.0 C. (f) Cycling performance of S@Co/Co_3O_4-NHC with a sulfur loading of 4 mg cm^{-2} at 1C for 250 cycles. (g) Long-term cycling performance of S@Co/Co_3O_4-NHC, S@NHC, and S@Co-NC electrodes at 1C for 500 cycles. (h) UV-vis absorption spectra of 10 mM Li_2S_6 solutions containing Co/Co_3O_4-NHC, NHC, and Co-NC. Inset is the digital photos of Li_2S_6 solutions after 24 h stirring.

Conflict of Interest

The authors declare no conflict of interest.

Acknowledgements

This research was supported by the Basic Science Research Program through the National Research Foundation of Korea (NRF) funded by the Ministry of Education (NRF-2018R1D1A1B07051249), Nano Material Technology Development Program (NRF-2015M3A7B6027970), Science and Technology Amicable Relationships (STAR) Program (NRF-2019K1A3A1A21031052) of MSIT/NRF, and the Hong Kong Polytechnic University (1-BE0Y). This research was also supported by the Center for Integrated Smart Sensors funded by the Ministry of Science, ICT and Future Planning, Republic of Korea, as Global Frontier Project (CISS-2012M3A6A6054186).

References

[1] A. Manthiram, Materials challenges and opportunities of lithium ion batteries, A. J. Phys. Chem. Lett. 2 (2011) 176-184.

[2] J.B. Goodenough, Y. Kim, Challenges for rechargeable Li batteries, Chem. Mater. 22 (2010) 587-603.

[3] M. Armand, J.M. Tarascon, Building better batteries, Nat. 451 (2008) 652-657.

[4] A. Manthiram, Y. Fu, S.H. Chung, C. Zu, Y.S. Su, Rechargeable lithium-sulfur batteries, Chem. Rev. 114 (2014) 11751-11787.

[5] P.G. Bruce, S.A. Freunberger, L.J. Hardwick, J.M. Tarascon, Li-O_2 and Li-S batteries with high energy storage, Nat. Mater. 11 (2011) 19-29.

[6] X. Ji, L.F. Nazar, Advances in Li–S batteries, J. Mater. Chem. 20 (2010) 9821-9826.

[7] X. Wu, N. Liu, Z. Guo, M. Wang, Y. Qiu, D. Tian, B. Guan, L. Fan, N. Zhang, Constructing multi-functional Janus separator toward highly stable lithium batteries, Energy Strorage Mater. 28 (2020) 153-159.

[8] M. Wang, L. Fan, X. Sun, B. Guan, B. Jiang. X. Wu, D. Tian, K. Sun, Y. Qiu, X. Yin, Y. Zhang, N. Zhang, Nitrogen Doped $CoSe_2$ as a bifunctional catalyst for high areal capacity and lean electrolyte of Li-S battery, ACS Energy Lett. (2020), 10.1021/acsenergylett.0c01564.

[9] Y. Fu, C. Zu, A. Manthiram, In situ-formed Li_2S in lithiated graphite electrodes for lithium-sulfur batteries, J. Am. Chem. Soc. 135 (2013) 18044-18047.

[10] Y. Yang, G. Zheng, S. Misra, J. Nelson, M.F. Toney, Y. Cui, High-capacity micrometer-sized Li_2S particles as cathode materials for advanced rechargeable lithium-ion batteries, J. Am. Chem. Soc. 134 (2012) 15387-15394.

[11] H. Chu, H. Noh, Y.J. Kim, S. Yuk, J.H. Lee, J. Lee, H. Kwack, Y. Kim, D.K. Yang, H.T. Kim, Achieving three-dimensional lithium sulfide growth in lithium-sulfur batteries using high-donor-number anions, Nat. Commun. 10 (2019) 188.

[12] D. Zheng, G. Wang, D. Liu, J. Si, T. Ding, D. Qu, X. Yang, D. Qu, The progress of Li-S batteries-understanding of the sulfur redox mechanism: dissolved polysulfide ions in the electrolytes, Adv. Mater. Technol. 3 (2018) 1700233.

[13] Y.V. Mikhaylik, J.R. Akridge, Polysulfide shuttle study in the Li/S battery system, J. Electrochem. Soc. 151 (2004) A1969-A1976.

[14] R.D. Rauh, F.S. Shuker, J.M. Marston, S.B. Brummer, Formation of lithium polysulfides in aprotic media, J. Inorg. Nucl. Chem. 39 (1977) 1761-1766.

[15] S.S. Li, B. Jin, X.J. Zhai, H. Li, Q. Jiang, Review of carbon materials for lithium-sulfur batteries, ChemistrySelect 3 (2018) 2245-2260.

[16] Z.L. Xu, J.K. Kim, K. Kang, Carbon nanomaterials for advanced lithium sulfur batteries, Nano Today 19 (2018) 84-107.

[17] L. Ji, M. Rao, S. Aloni, L. Wang, E.J. Cairns, Y. Zhang, Porous carbon nanofiber–sulfur composite electrodes for lithium/sulfur cells, Energy Environ. Sci. 4 (2011) 5053-5059.

[18] J. Guo, Y. Xu, C. Wang, Sulfur-impregnated disordered carbon nanotubes cathode for lithium-sulfur batteries, Nano Lett. 11 (2011) 4288-4294.

[19] Y. Zhao, W. Wu, J. Li, Z. Xu, L. Guan, Encapsulating MWNTs into hollow porous carbon nanotubes: a tube-in-tube carbon nanostructure for high-performance lithium-sulfur batteries, Adv. Mater. 26 (2014) 5113-5118.

[20] N. Jayaprakash, J. Shen, S.S. Moganty, A. Corona, L.A. Archer, Porous hollow carbon@sulfur composites for high-power lithium-sulfur batteries, Angew. Chem. Int. Ed. Engl. 50 (2011) 5904-5908.

[21] C. Zhang, H.B. Wu, C. Yuan, Z. Guo, X.W. Lou, Confining sulfur in double-shelled hollow carbon spheres for lithium-sulfur batteries, Angew. Chem. Int. Ed. Engl. 51 (2012) 9592-9595.

[22] Z. Li, Y. Jiang, L.X. Yuan, Z.Q. Yi, C. Wu, Y. Liu, P. Strasser, Y.H. Huang, A highly ordered meso@microporous carbon-supported sulfur@smaller sulfur core-shell structured cathode for Li-S batteries, ACS Nano 8 (2014) 9295-9303.

[23] Z. Zeng, X. Liu, Sulfur immobilization by “chemical anchor” to suppress the diffusion of polysulfides in lithium-sulfur batteries, Adv. Mater. Interfaces 5 (2018) 1701274.

[24] C. Li, Z. Xi, D. Guo, X. Chen, L. Yin, Chemical immobilization effect on lithium polysulfides for lithium-sulfur batteries, Small 14 (2018) 1701986.

[25] J. Xu, T. Lawson, H. Fan, D. Su, G. Wang, Updated metal compounds (MOFs, −S, −OH, −N, −C) used as cathode materials for lithium-sulfur batteries, Adv. Energy Mater. 8 (2018) 1702607.

[26] M. Kim, J. Lee, Y. Jeon, Y. Piao, Phosphorus-doped graphene nanosheets anchored with cerium oxide nanocrystals as effective sulfur hosts for high performance lithium-sulfur batteries, Nanoscale 11 (2019) 13758-13766.

[27] J. Wu, Q. Ma, C. Lian, Y. Yuan, D. Long, Promoting polythionate intermediates formation by oxygen-deficient manganese oxide hollow nanospheres for high performance lithium-sulfur batteries, Chem. Eng. J. 370 (2019) 556-564.

[28] Z. Wei Seh, W. Li, J.J. Cha, G. Zheng, Y. Yang, M.T. McDowell, P.C. Hsu, Y. Cui, Sulphur-TiO_2 yolk-shell nanoarchitecture with internal void space for long-cycle lithium-sulphur batteries, Nat. Commun. 4 (2013) 1331.

[29] Q. Pang, D. Kundu, M. Cuisinier, L.F. Nazar, Surface-enhanced redox chemistry of polysulphides on a metallic and polar host for lithium-sulphur batteries, Nat. Commun. 5 (2014) 4759.

[30] J.R. He, G. Hartmann, M. Lee, G.S. Hwang, Y.F. Chen, A. Manthiram, Freestanding 1T MoS_2/graphene heterostructures as a highly efficient electrocatalyst for lithium polysulfides in Li-S batteries, Energy Environ. Sci. 12 (2019) 344-350.

[31] C. Dai, J.-M. Lim, M. Wang, L. Hu, Y. Chen, Z. Chen, H. Chen, S.-J. Bao, B. Shen, Y. Li, G. Henkelman, M. Xu, Honeycomb-like spherical cathode host constructed from hollow metallic and polar Co_9S_8 tubules for advanced lithium-sulfur batteries, Adv. Funct. Mater. 28 (2018) 1704443.

[32] H.B. Wu, S. Wei, L. Zhang, R. Xu, H.H. Hng, X.W. Lou, Embedding sulfur in MOF-derived microporous carbon polyhedrons for lithium-sulfur batteries, Chem. Eur. J. 19 (2013) 10804-10808.

[33] Y. Zheng, S.S. Zheng, H.G. Xue, H. Pang, Metal-organic frameworks for lithium-sulfur batteries, J. Mater. Chem. A 7 (2019) 3469-3491.

[34] A.E. Baumann, D.A. Burns, J.C. Diaz, V.S. Thoi, Lithiated defect sites in Zr metal-organic framework for enhanced sulfur utilization in Li-S batteries, ACS Appl. Mater. Interfaces 11 (2019) 2159-2167.

[35] X.J. Hong, C.L. Song, Y. Yang, H.C. Tan, G.H. Li, Y.P. Cai, H.X. Wang, Cerium based metal-organic frameworks as an efficient separator coating catalyzing the conversion of polysulfides for high performance lithium-sulfur batteries, ACS Nano 13 (2019) 1923-1931.

[36] P.B. Geng, S. Cao, X.T. Guo, J.W. Ding, S.T. Zhang, M.B. Zheng, H. Pang, Polypyrrole coated hollow metal-organic framework composites for lithium-sulfur batteries, J. Mater. Chem. A 7 (2019) 19465-19470.

[37] Z.Q. Li, C.X. Li, X.L. Ge, J.Y. Ma, Z.W. Zhang, Q. Li, C.X. Wang, L.W. Yin, Reduced graphene oxide wrapped MOFs-derived cobalt-doped porous carbon polyhedrons as sulfur immobilizers as cathodes for high performance lithium sulfur batteries, Nano Energy 23 (2016) 15-26.

[38] H.N. Yu, B. Zhang, F.G. Sun, G.Y. Jiang, N. Zheng, C.P. Xu, Y.S. Li, Core-shell polyhedrons of carbon nanotubes-grafted graphitic carbon@nitrogen doped carbon as efficient sulfur immobilizers for lithium-sulfur batteries, Appl. Surf. Sci. 450 (2018) 364-371.

[39] Y.-J. Li, J.-M. Fan, M.-S. Zheng, Q.-F. Dong, A novel synergistic composite with multi-functional effects for high-performance Li–S batteries, Energy Environ. Sci. 9 (2016) 1998-2004.

[40] Z. Chang, B. Ding, H. Dou, J. Wang, G.Y. Xu, X.G. Zhang, Hierarchically porous multilayered carbon barriers for high-performance Li-S Batteries, Chem. Eur. J. 24 (2018) 3768-3775.

[41] Y. Pan, K. Sun, S. Liu, X. Cao, K. Wu, W.C. Cheong, Z. Chen, Y. Wang, Y. Li, Y. Liu, D. Wang, Q. Peng, C. Chen, Y. Li, Core-shell ZIF-8@ZIF-67-derived CoP nanoparticle-embedded N-doped carbon nanotube hollow polyhedron for efficient overall water splitting, J. Am. Chem. Soc. 140 (2018) 2610-2618.

[42] J. Kim, C. Young, J. Lee, Y.-U. Heo, M.-S. Park, M.S.A. Hossain, Y. Yamauchi, J.H. Kim, Nanoarchitecture of MOF-derived nanoporous functional composites for hybrid supercapacitors, J. Mater. Chem. A 5 (2017) 15065-15072.

[43] J. Zhang, T. Zhang, K. Xiao, S. Cheng, G. Qian, Y. Wang, Y. Feng, Novel and facile strategy for controllable synthesis of multilayered core–shell zeolitic imidazolate frameworks, Cryst. Growth Des. 16 (2016) 6494-6498.

[44] A. Diallo, A.C. Beye, T.B. Doyle, E. Park, M. Maaza, Green synthesis of Co_3O_4 nanoparticles via aspalathus linearis: physical properties, Green Chem. Lett. Rev. 8 (2015) 30-36.

[45] S. Farhadi, M. Javanmard, G. Nadri, Characterization of cobalt oxide nanoparticles prepared by the thermal decomposition, Acta Chim. Slov. (2016) 335-343.

[46] J. Xu, W.X. Zhang, Y. Chen, H.B. Fan, D.W. Su, G.X. Wang, MOF-derived porous N-Co_3O_4@N-C nanododecahedra wrapped with reduced graphene oxide as a high capacity cathode for lithium-sulfur batteries, J. Mater. Chem. A 6 (2018) 2797-2807.

[47] L. Zhou, H. Li, X. Wu, Y. Zhang, D.L. Danilov, R.-A. Eichel, P.H.L. Notten, double-shelled Co_3O_4/C nanocages enabling polysulfides adsorption for high-performance lithium–sulfur batteries, ACS Appl. Energy Mater. 2 (2019) 8153-8162.

[48] N.K. Chaudhari, M.-S. Kim, T.-S. Bae, J.-S. Yu, Hematite (α-Fe_2O_3) nanoparticles on vulcan carbon as an ultrahigh capacity anode material in lithium ion battery, Electrochim. Acta 114 (2013) 60-67.

[49] J. Lee, S.-K. Park, Y. Piao, N-doped carbon framework/reduced graphene oxide nanocomposite as a sulfur reservoir for lithium-sulfur batteries, Electrochim. Acta 222 (2016) 1345-1353.

[50] Z.Q. Li, L.W. Yin, Nitrogen-Doped MOF-Derived Micropores Carbon as Immobilizer for Small Sulfur Molecules as a Cathode for Lithium Sulfur Batteries with Excellent Electrochemical Performance, ACS Appl. Mater. Inter. 7 (2015) 4029-4038.

[51] Y.C. Qiu, W.F. Li, W. Zhao, G.Z. Li, Y. Hou, M.N. Liu, L.S. Zhou, F.M. Ye, H.F. Li, Z.H. Wei, S.H. Yang, W.H. Duan, Y.F. Ye, J.H. Guo, Y.G. Zhang, High-Rate, Ultra long Cycle-Life Lithium/Sulfur Batteries Enabled by Nitrogen-Doped Graphene, Nano Letters 14 (2014) 4821-4827.

[52] Z. Yu, Y. Bai, Y. Liu, S. Zhang, D. Chen, N. Zhang, K. Sun, Metal-organic-framework-derived yolk-shell-structured cobalt-based bimetallic oxide polyhedron with high activity for electrocatalytic oxygen evolution, ACS Appl. Mater. Interfaces 9 (2017) 31777-31785.

[53] X. Xiong, G. Waller, D. Ding, D. Chen, B. Rainwater, B. Zhao, Z. Wang, M. Liu, Controlled synthesis of $NiCo_2S_4$ nanostructured arrays on carbon fiber paper for high-performance pseudocapacitors, Nano Energy 16 (2015) 71-80.

[54] H. Zhang, L.G. Wang, Q. Li, L. Ma, T.P. Wu, Y.L. Ma, J.J. Wang, C.Y. Du, G.P. Yin, P.J. Zuo, Cobalt nanoparticle-encapsulated carbon nanowire arrays: Enabling the fast redox reaction kinetics of lithium-sulfur batteries, Carbon 140 (2018) 385-393.

[55] Y. Hou, J.Y. Li, X.F. Gao, Z.H. Wen, C. Yuan, J.H. Chen, 3D dual-confined sulfur encapsulated in porous carbon nanosheets and wrapped with graphene aerogels as a cathode for advanced lithium sulfur batteries, Nanoscale 8 (2016) 8228-8235.

[56] Y.T. Liu, D.D. Han, L. Wang, G.R. Li, S. Liu, X.P. Gao, $NiCo_2O_4$ nanofibers as carbon-free sulfur immobilizer to fabricate sulfur-based composite with high volumetric capacity for lithium-sulfur battery, Adv. Energy Mater. 9 (2019) 1803477.

[57] X. Tao, J. Wang, C. Liu, H. Wang, H. Yao, G. Zheng, Z.W. Seh, Q. Cai, W. Li, G. Zhou, C. Zu, Y. Cui, Balancing surface adsorption and diffusion of lithium-polysulfides on nonconductive oxides for lithium-sulfur battery design, Nat. Commun. 7 (2016) 11203.

[58] A. Benitez, A. Caballero, J. Morales, J. Hassoun, E. Rodriguez-Castellon, J. Canales-Vazquez, Physical activation of graphene: An effective, simple and clean procedure for obtaining microporous graphene for high-performance Li/S batteries, Nano Res. 12 (2019) 759-766.

For Table of Contents Only